

Flexible and Stretchable 3ω Sensors for Thermal Characterization of Human Skin

Limei Tian, Yuhang Li, Richard Chad Webb, Siddharth Krishnan, Zuguang Bian, Jizhou Song, Xin Ning, Kaitlyn Crawford, Jonas Kurniawan, Andrew Bonifas, Jun Ma, Yuhao Liu, Xu Xie, Jin Chen, Yuting Liu, Zhan Shi, Tianqi Wu, Rui Ning, Daizhen Li, Sanjiv Sinha, David G. Cahill, Yonggang Huang,* and John A. Rogers*

Characterization of the thermal properties of the surface and subsurface structures of the skin can reveal the degree of hydration, the rate of blood flow in near-surface micro- and macrovasculature, and other important physiological information of relevance to dermatological and overall health status. Here, a soft, stretchable thermal sensor, based on the so-called three omega (i.e., 3ω) method, is introduced for accurate characterization of the thermal conductivity and diffusivity of materials systems, such as the skin, which can be challenging to measure using established techniques. Experiments on skin at different body locations and under different physical states demonstrate the possibilities. Systematic studies establish the underlying principles of operation in these unusual systems, thereby allowing rational design and use, through combined investigations based on analytical modeling, experimental measurements, and finite element analysis. The findings create broad opportunities for 3ω methods in biology, with utility ranging from the integration with surgical tools or implantable devices to noninvasive uses in clinical diagnostics and therapeutics.

1. Introduction

A widely adopted method for evaluating the thermal properties of materials involves application of an oscillating current with frequency of ω to a resistive thermal actuator, with simultaneous measurement of the oscillating component of the voltage drop at a frequency of 3ω that follows from nonlinearities associated with the temperature dependence of the resistance. This approach, known as the 3ω technique, provides a precise and accurate means for determining the thermal transport properties of bulk materials and thin films, as described in many reports over the last 25 years.^[1-3] Recent efforts involve application to biological samples (100 μm to 3 mm thick slices of liver and cardiac

Dr. L. Tian
Beckman Institute for Advanced Science and Technology
University of Illinois at Urbana-Champaign
Urbana, IL 61801, USA

Dr. Y. Li, J. Chen
Institute of Solid Mechanics
Beihang University (BUAA)
Beijing 100191, China

Dr. R. C. Webb, S. Krishnan, Dr. X. Ning, Dr. K. Crawford,
J. Kurniawan, Dr. A. Bonifas, Dr. Y. Liu, Dr. X. Xie, Y. Liu,
Z. Shi, R. Ning, D. Li
Department of Materials Science and Engineering
Frederick Seitz Materials Research Laboratory
University of Illinois at Urbana-Champaign
Urbana, IL 61801, USA

Dr. Z. Bian
Ningbo Institute of Technology
Zhejiang University
Ningbo 315100, China

Dr. J. Song
Department of Engineering Mechanics
Zhejiang University
Hangzhou, Zhejiang 310027, China

J. Ma, Prof. S. Sinha
Department of Mechanical Science and Engineering
University of Illinois at Urbana-Champaign
Urbana, IL 61801, USA

T. Wu
Department of Industrial and Enterprise Systems Engineering
University of Illinois at Urbana-Champaign
Urbana, IL 61801, USA

Prof. D. G. Cahill
Department of Materials Science and Engineering
University of Illinois at Urbana-Champaign
Urbana, IL 61801, USA

Prof. Y. Huang
Departments of Civil and Environmental Engineering and Mechanical
Engineering, Center for Engineering and Health, and Skin Disease
Research Center
Northwestern University
Evanston, IL 60208, USA
E-mail: y-huang@northwestern.edu

Prof. J. A. Rogers
Department of Materials Science and Engineering
Chemistry, Mechanical Science and Engineering, Electrical
and Computer Engineering, Beckman Institute for Advanced Science
and Technology, and Frederick Seitz Materials Research Laboratory
University of Illinois at Urbana-Champaign
Urbana, IL 61801, USA
E-mail: jrogers@northwestern.edu

DOI: 10.1002/adfm.201701282

tissue obtained using *ex vivo* preparations) using 3ω sensors constructed on rigid planar substrates.^[4–6] The implementation of sensors constructed in soft, flexible, and stretchable forms could create opportunities for direct, *in vivo* measurements on the soft, curved tissues of living organisms.^[7–14]

Simple thermal characterization devices previously reported constructed using the principles of stretchable electronics can measure various thermal transport properties of human skin. Previously reported demonstrations include the assessment of hydration state, blood flow, and other parameters of clinical interest using direct current (DC) approaches.^[15–17] The transient plane source analysis methods used in these cases require careful calibration against materials with known thermal properties under controlled measurement environments.^[15,17] By comparison, alternating current (AC) methods, such as the 3ω technique, are much easier to implement accurately in practice by using frequency to confine the thermal penetration depth in the sample under test. Furthermore, responses associated with localized thermal actuation are comparatively less sensitive to boundary conditions between the material under test and its substrate and to characteristics of the surrounding environment, by their avoidance of DC voltage artifacts that arise from thermoelectric effects and low-frequency drifts, and from radiative and convection loss mechanisms.^[18] The heating frequency in AC methods can be tuned to control the thermal penetration depth, which enables the thermal properties measurements of multilayer structures.^[19]

For these reasons, implementation of 3ω techniques using soft, conformal devices applied to biological tissues is of interest. Thermal characterization of the skin, in particular, can reveal changes in both structure and activity, each in physical and chemical states relevant to dermatological health. For instance, the degree of skin hydration and the rate of blood flow in near-surface vasculature can be inferred from thermal properties.^[15,16,20] Most existing methods for *in vivo* thermal evaluation of skin rely either on complex optical setups, in the case of photothermal techniques and infrared thermography methods, or they require bulky, rigid probes that are applicable to only certain regions of the skin.^[21,22] The following introduces designs for flexible and stretchable 3ω sensors, along with systematic studies of the physics associated with their use in characterization of thermal conductivity and diffusivity of various materials, including skin on different body locations.

Compared to standard plane source methods designed for measurements of biological materials, the 3ω technique eliminates important artifacts, and it improves robustness in operation and ease in implementation. Leveraging 3ω measurements with soft, removable device platforms demands stretchable, serpentine designs in the active elements, and a full accounting of the resulting self-proximity effects induced by propagating thermal waves. The present manuscript examines these effects in a systematic set of experimental and computational efforts, and uses the results to establish foundational design rules for the devices. Finite element computational methods ensure a high level of accuracy in analysis of the measurement results, by capturing the superposition of thermal signals and the influence of the layered structures in the devices. Additionally, optimized layouts in the serpentine geometries, guided by mechanics modeling, provide much larger levels of elastic

stretchability along all directions (>50%) than possible in previously reported plane source thermal characterization platforms (~15%). The results establish guidelines for rational design and use of these types of devices, through combined investigations based on analytical modeling, experimental measurements, and finite element analysis. The findings create broad opportunities for the use of 3ω methods in biology.

2. Results and Discussion

Most 3ω measurements use simple, thin film resistive heating elements based on metals with straight, linear geometries, on rigid planar substrates. Such layouts and materials do not, however, offer the effective low modulus, elastic mechanics needed to conform to curved, time dynamic surfaces found in biology, simply because strains larger than a few percent applied in the direction parallel to the long axis of the heater element will lead to plastic deformation and fracture. By contrast, filamentary heater structures in serpentine, self-similar, and/or fractal geometries provide excellent levels of stretchability when integrated with soft, elastomeric substrates, simply due to in and out-of-plane buckling motions that allow globally deformation without inducing high levels of strain in the metal.^[23,24] The example in Figure 1a uses a serpentine filament, consisting of a trace of Au (5 μ m wide and 100 nm thick) encapsulated on top and bottom by films of polyimide (PI, 20 μ m wide and 0.9 μ m thick), mounted on a silicone sheet (Ecoflex, elastic modulus of 60 kPa, and width, length and thickness of 2 cm, 3 cm, and 100 μ m, respectively). The image shows the device laminated onto the curved surface of the skin of the forearm. Lead wires provide a four-point measurement configuration (Figure 1b). The PI serves as electrical insulation, biofluid protection, and strain isolation of the metal by its location near the neutral mechanical plane (Figure 1c). Passing a sinusoidal current at a frequency 1ω (AC current source; Keithley 6221, USA) generates heating in the metal that causes oscillations in the voltage drop. A digital lock-in amplifier (SR830, Stanford Research Systems, USA) captures the third harmonic of this measured response. As a reference to study the operation, infrared imaging can capture the induced oscillations in temperature from a 3ω sensor actuated with current with a root mean square magnitude of 3 mA at a frequency of 0.1 Hz (Figure 1d). Temperatures in the heating area show a periodic fluctuation of ~10 °C at 0.2 Hz (Figure 1e).

Such types of measurements can be used in two straightforward, but important, functions in the context of skin or other biologically related applications. The simplest is as a contact sensor, as shown in Figure 1f. Here, changes in the first and third harmonic voltages at a measurement frequency of 250 Hz result from changes in the quality of skin contact and resultant changes in the thermal transport away from the sensor. As expected, both first and third harmonic voltages decrease upon contact, due to the increase in the thermal transport that follows from replacement of air with skin. The change in voltage at 3ω is ~22%, which is more than a factor of 20 higher than that at 1ω (0.9%). Furthermore, the response time associated with measurements at 3ω is shorter than that at 1ω . These dramatic differences can serve as an initial indication of contact

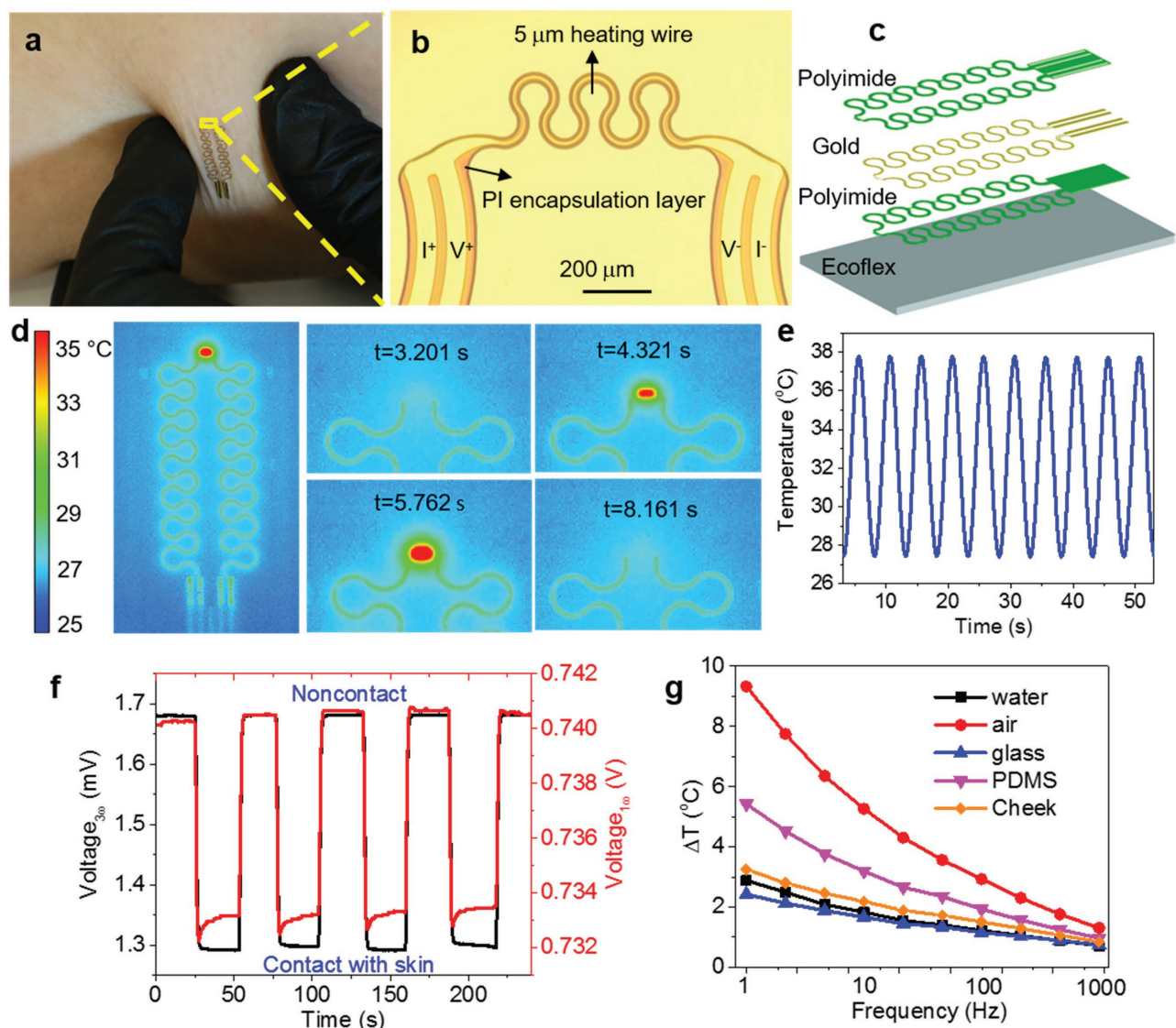


Figure 1. Flexible and stretchable 3ω sensors. a) Photograph of a serpentine 3ω sensor printed onto a thin silicone substrate and applied to the skin of forearm of a subject. b) Optical image of a serpentine wire composed of an Au heater (5 μm wide) and PI encapsulation layers (20 μm wide). c) Exploded-view schematic illustration of different layers in the devices. PI layers encapsulate the Au wires from the environment, and also provide mechanical support. d) Infrared thermal images show the temperature oscillations for a serpentine heater supplied with an input AC current of 3 mA at 0.1 Hz. e) Temperature oscillations measured at the heater area in (d). f) 3ω sensor as an epidermal contact sensor showing the changes of voltages at frequencies 1ω and 3ω under contact and noncontact states, respectively. g) Temperature oscillations measured from various materials with a fixed power input of 1.34 W m^{-1} at a wide range of frequencies from 1 to 1000 Hz. Except special note, all the temperatures represent the magnitude including in-phase and out-of-phase components, and the specific components are included in the Supporting Information.

quality during measurements in the second mode, which involves direct determination of thermal conductivity and diffusivity. Figure 1g shows examples of temperature fluctuations of various materials measured using 3ω sensors at different frequencies with the same power input (1.34 W m^{-1}), from which the thermal conductivity and diffusivity can be calculated accordingly, as described subsequently.

While previously published principles establish the foundations of 3ω techniques,^[1,5,18,25] several additional effects must be considered in the design and use of stretchable 3ω sensors designed to be reversibly laminated against a target material for testing. Using a simple straight wire configuration as a model,

systematic studies reveal the important design parameters, including the in-plane and cross-plane dimensions of the resistive wire and the encapsulating layers and the thickness of the soft support. As shown in the optical microscope images of Figure 2a, the investigations involve 3ω sensors with different dimensions, operated at frequencies across a range from 1 to 1000 Hz. Specifically, the sensors consist of straight Au wires with different widths (5 and 50 μm), PI encapsulation layers of different widths (20 and 60 μm) and thicknesses (0.9 and 2 μm), and silicone substrates with different thicknesses (10 to 250 μm) (Figure 2b). Unlike typical 3ω sensors, which use heating elements formed directly on the surface of a sample of

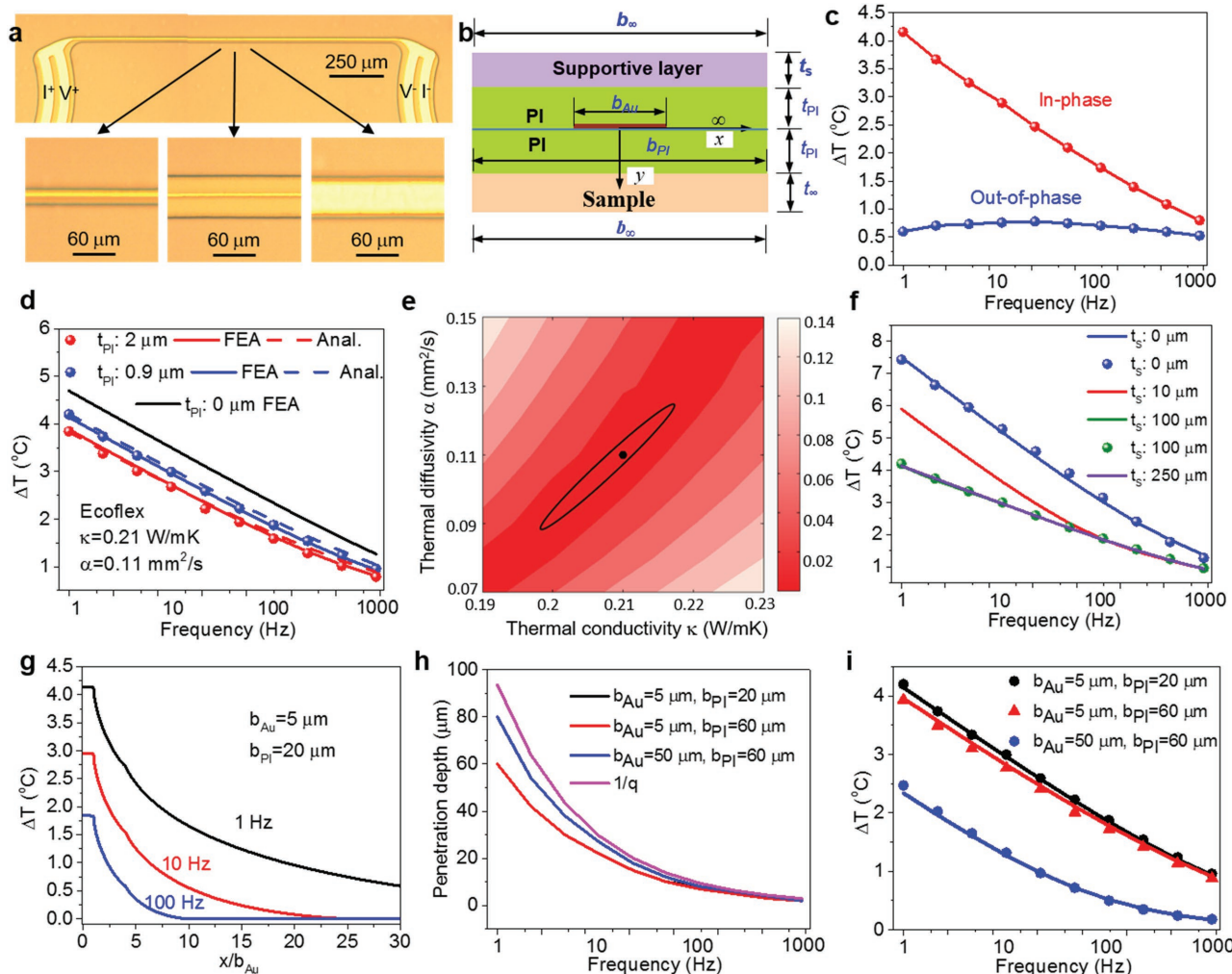


Figure 2. Device design considerations in 3ω sensors using a straight line geometry as a model. a) Optical images of straight line heaters, composed of Au and PI with different dimensions. b) Cross-sectional illustration of the sensor geometry. c) In-phase and out-of-phase temperature oscillations as a function of the logarithm of the frequency, measured from a straight wire composed of $5\text{ }\mu\text{m}$ wide Au heater and $20\text{ }\mu\text{m}$ wide PI layer. d) Comparison of temperature oscillations determined by experimental results, analytical calculation and FEA modeling for a straight wire geometry with different thicknesses of PI encapsulation layers across a frequency range of $1\text{--}1000\text{ Hz}$. e) The thermal conductivity and diffusivity of the soft silicone support were calculated to be $0.21 \pm 0.01\text{ W mK}^{-1}$ and $0.11 \pm 0.02\text{ mm}^2\text{ s}^{-1}$ using FEA and a relative least square method. Scale bar represents the sum of the standard deviation between ΔT_{Exp} and ΔT_{FEA} at all frequencies (i.e., σ). f) Comparison of temperature oscillations determined by experimental results and FEA modeling for devices with different thicknesses of the supporting silicone layers across a frequency range of $1\text{--}1000\text{ Hz}$. g) Magnitude of the temperature oscillation as a function of distance away from the heater, determined by FEA for $5\text{ }\mu\text{m}$ wide Au heater and $20\text{ }\mu\text{m}$ wide PI layer. h) Calculated thermal penetration depth provided by different widths of the Au heater and PI layer, comparing to an ideal value of $1/q$ with negligible edge effect. i) Comparison of temperature oscillations determined by experimental results and FEA modeling for devices with different widths of Au wires and PI layers. Dots represent experimental results; dashed lines represent analytical solutions and solid lines represent FEA. Except (c), all the temperatures represent the magnitude including in-phase and out-of-phase components, and the specific components are included in the Supporting Information.

interest, here the devices softly laminate on this surface, and then subsequently can be removed for repeated measurements.

In a four-point measurement configuration, sinusoidal current applied to the heater results in a third harmonic in the voltage signal. Specifically, current at frequency 1ω causes Joule heating at a rate that has frequency components at DC (0 Hz) and 2ω . The temperature dependence of the electrical resistance of the heater leads to a variation at 2ω with an amplitude and phase that depend on the thermal properties of the surroundings. These oscillations in resistance, at 2ω , combine with the drive current at 1ω to create oscillations in voltage across the

heater at a frequency of 3ω , measurable with a lock-in amplifier. The temperature oscillation averaged across the width of the line-heater can be experimentally measured in this manner. Calculations use the calibrated temperature coefficient of resistance dT/dR and the third harmonic voltage V_3 according to ref. [1]

$$\overline{\Delta T} = \frac{P}{l\pi k} \int_0^\infty \frac{\sin^2(vb)}{(vb)^2(v^2+q^2)^{1/2}} dv = 2 \frac{dT}{dR} \frac{V_3}{I} \quad (1)$$

where P is the power, l is the heater length, k is the thermal conductivity of the substrate, b is the half-width of the line-heater,

ν represents the Fourier space, dT/dR is the temperature coefficient of resistance of the line-heater, V_3 is the measured voltage at the third harmonic, I is the current, and the magnitude of $1/q$ is the thermal penetration depth defined as^[1]

$$\frac{1}{q} = \left(\frac{\alpha}{i2\omega} \right)^{1/2} \quad (2)$$

where α is the thermal diffusivity and ω is the frequency in radians.

Initial measurements and calculations focus on in-phase and out-of-phase temperature oscillations of a heater in a sensor that consists of an Au wire (5 μm wide) with PI encapsulation layers (20 μm wide and 0.9 μm thick) on a silicone substrate (100 μm thick), and is placed on another layer of silicone (100 μm thick) as a measurement sample (Figure 2c). The in-phase temperature oscillations increase in amplitude in a linear fashion with a decrease in the logarithm of the operating frequency $\ln(\omega)$. By contrast, the out-of-phase temperature oscillations are approximately constant, as expected from previous studies in the literature.^[1] Temperature oscillations obtained from experimental measurements and Equation (1) serve as the input for finite element analysis (FEA) approaches designed to determine the thermal conductivity and diffusivity, in an iterative process that minimizes the parameter σ , defined as

$$\sigma = \sqrt{\sum_n \left(\frac{\Delta T_{\text{Exp}} - \Delta T_{\text{FEA}}}{\Delta T_{\text{Exp}}} \right)^2} \quad (3)$$

where ΔT_{Exp} and ΔT_{FEA} represent the temperature oscillations of Au wire obtained in the experiments and FEA, respectively. The thermal conductivity and diffusivity correspond to the values that minimize the sum of the standard deviation between ΔT_{Exp} and ΔT_{FEA} at all frequencies (i.e., σ_{min}). The results for the case described above yield $0.21 \pm 0.01 \text{ W mK}^{-1}$ and $0.11 \pm 0.02 \text{ mm}^2 \text{ s}^{-1}$ for the silicone sample (Figure 2e). The calculated values are consistent with the results of silicone materials reported in literature, thereby validating the scheme.^[26] The contour line in Figure 2e indicates the uncertainties of thermal conductivity and diffusivity based on the goodness of fit with a deviation summation $1.4\sigma_{\text{min}}$. The uncertainties of thermal conductivity and diffusivity are 5% and 18%, respectively, which derive from noise and other imperfections in the measured temperature oscillations. Systematic uncertainty was estimated to be 4%, including uncertainties of the dimension of Au heater and PI encapsulation layer and temperature coefficient of resistance.

Comparisons between experimental and theoretical results obtained by analytical modeling (Supporting information) and FEA for devices with various thicknesses of PI appear in Figure 2d. As revealed in Figure 2d, temperature oscillations increase with decreasing PI thickness mainly due to the higher thermal conductivity of PI than silicone.^[26,27] Overall, experimental results (represented as dots) agree well with analytical solutions (dashed lines) and FEA values (solid lines) at all frequencies. Further validation of FEA models and calculations follow from comparisons against previous methods,^[1] in which the thermal conductivity can be extracted from the slope of

the in-phase component of the temperature oscillation versus $\ln(\omega)$. Oscillations in the range of 10–100 Hz minimize errors created by radiation effects at low frequencies and by thermal barrier effects associated with the PI at high frequencies. The thermal conductivity of the silicone extracted in this manner is 0.21 W mK^{-1} , in agreement with the FEA value determined by fitting. We also measured and calculated the thermal property of many other polymeric materials, which show good agreement with reported values (Figure S2, Table S1, Supporting Information).

The effects of the silicone support can also be important (Figure 2f). Experimental results and FEA values reveal that the temperature oscillations increase with decreasing thickness of this support, especially at low frequencies due to the comparatively large thermal penetration depths in this range. For thicknesses greater than 100 μm , however, the effects are small even at frequencies as low as 1 Hz, which follows the thermal penetration depth in silicone at 1 Hz is around 93 μm calculated using Equation (2). Measurements described subsequently use a silicone support of 100 μm thick.

The previous analyses indicate that changes in the thickness of the PI and soft support can alter the measured signal. The in-plane dimensions of the PI encapsulation and Au wire ($b_{\text{PI}} = 20\text{--}60 \mu\text{m}$, $b_{\text{Au}} = 5\text{--}50 \mu\text{m}$) can also be important, which can influence the thermal penetration depth due to the edge effect of Au heater. Typically, this depth depends on frequency, as shown in Equation (2). The thermal oscillation amplitude decreases with distance at rates that increase with frequency, as shown in Figure 2g. Figure 2h shows the computed thermal penetration depths provided by different Au heater and PI dimensions (see calculation details in Supporting Information). As expected, the penetration depth increases with the decrease in frequency. Due to different degrees of edge effect of Au heaters, the calculated penetration depths provided by 5 and 50 μm heaters are smaller than the ideal value of $1/q$ calculated using Equation (2). The 5 μm Au heater regardless the PI width, with larger edge effect, provides smaller penetration depth compared to the 50 μm Au heater. For a fixed input power of 1.34 W m^{-1} , the reduced amplitude in the temperature oscillations associated with the sensor with wide dimensions follows its reduced power density (Figure 2i). The 50 μm Au heater exhibits deviation from linear behavior in the frequency range of 4.5–1000 Hz due to the small value of the thermal penetration depth normalized by heater width less than one. By contrast, the 5 μm Au heater shows a linear trend in a large frequency range of 1–450 Hz, which simplifies the calculation. In practice, high frequencies offer advantages in speed of measurement and high sampling rates, often important and useful in biological experiments. All such considerations are relevant to the design of 3ω sensors, independent of in-plane geometries, including serpentine architectures described next.

As demonstrated in previous work on mechanics for stretchable electronics, for a given geometry, serpentine designs with a narrow wire width provides relatively large stretchability.^[28] Based on the effects outlined above, an optimized sensor design for measurements described in the following involves a small Au heater with width of 5 μm and similarly shaped pair of PI encapsulation layers with widths of 20 μm . An overall layout in the form of a filamentary serpentine structure

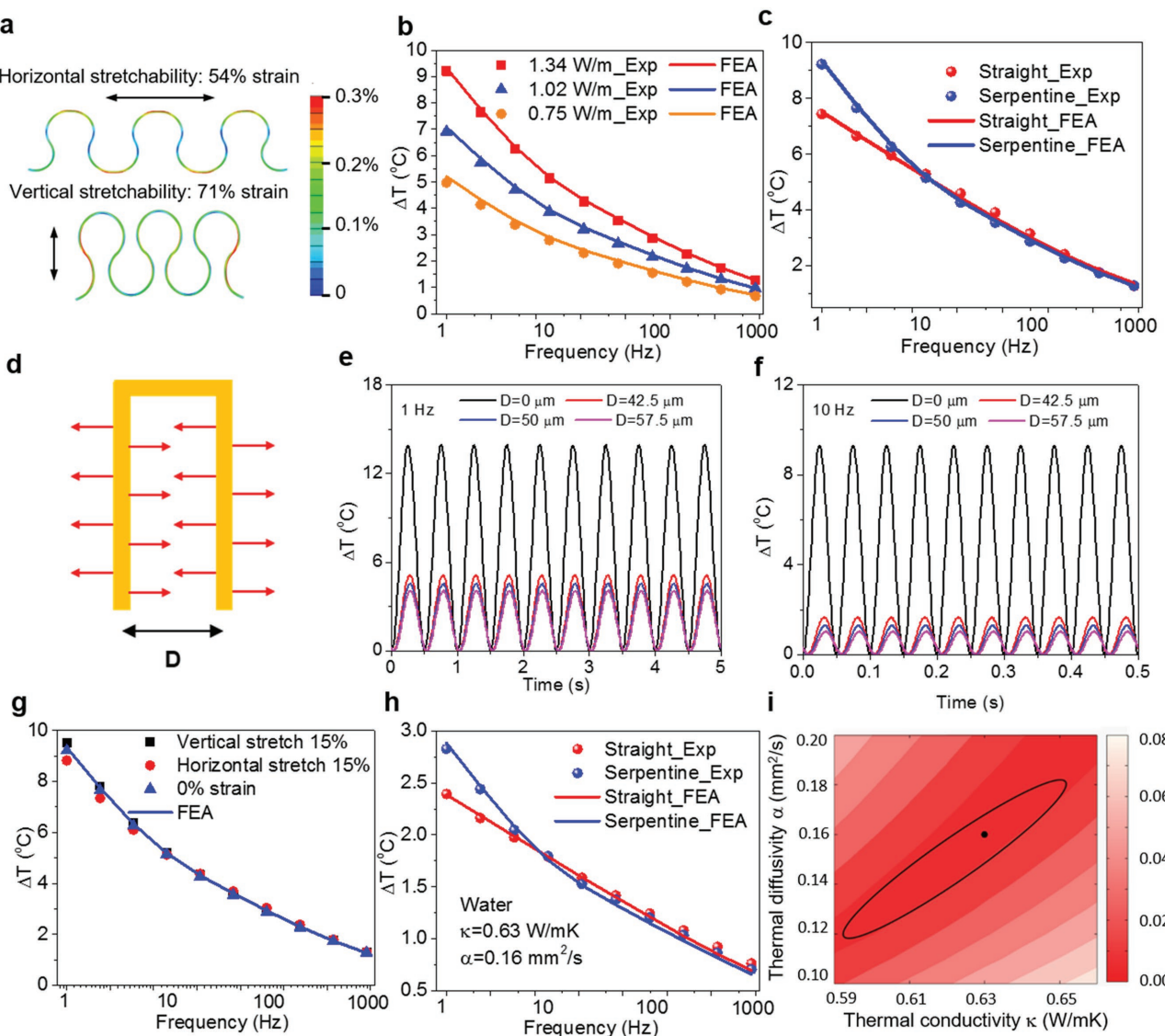


Figure 3. Serpentine designs in stretchable 3ω sensors. a) Computational results that indicate large elastic stretchability in a serpentine Au wire for stretching in both the horizontal and vertical directions. b) Temperature oscillation measured from the serpentine wire in air as a function of frequency with different power input, in good agreement with FEA. c) Comparisons between temperatures of serpentine and straight wire as a function of frequency, indicating only minor differences at high frequencies but higher values for the serpentine case at low frequencies (<10 Hz). d) A simplified model of a serpentine line-heater used to explain the differences in (c). e) Calculated temperature oscillations of a line-heater with a power input of 1.34 W m^{-1} and projected values at a distance $50 \mu\text{m}$ and $50 \pm 7.5 \mu\text{m}$ away for a frequency of 1 Hz and f) 10 Hz. g) Measured temperatures as a function of frequency from the serpentine wire with 15% global strain applied in the horizontal and vertical directions, respectively. h) Comparison of temperatures of serpentine and straight wire as a function of frequency measured on water. i) The extracted thermal conductivity and diffusivity of water are $0.63 \pm 0.04 \text{ W mK}^{-1}$ and $0.16 \pm 0.04 \text{ mm}^2 \text{ s}^{-1}$.

provides elastic stretchability of 54% and 71% in the horizontal and vertical directions, respectively, as computed by FEA with a threshold for Au plastic deformation of 0.3% (Figure 3a). For reference, human skin has a linear response to tensile strain up to $\approx 15\%$ and a failure strain at $>35\%$.^[29] The thermal oscillations of such 3ω sensors measured in air with various input powers, show good agreement with FEA results (Figure 3b). Unlike the linear configuration, the serpentine shape can lead to proximity effects, wherein thermal oscillations generated by one part of the sensor impinge onto an adjacent region. Temperature oscillations of 3ω sensors in serpentine and straight

wire geometries, further validated by FEA, appear in Figure 3c. Compared to the straight case, proximity effects in the serpentine lead to increased temperature oscillations at low frequencies (<10 Hz).

An approximate numerical analysis, presented in Figure 3d, illustrates the concept. Here, two, parallel line-heaters with half-widths of b and with the same oscillating current lie in proximity to one another. The thermal oscillation induced by one of the line-heaters within itself and at a distance D away can be approximated by numerical calculation. A combination of these two contributions defines the signal experienced by either wire

as a result of the proximity to the other. In particular, the signal can be calculated as

$$\Delta T(x,t) = A \frac{1 - \cos(2\omega t - \pi/4)}{2} + B \frac{1 - \cos\left(2\omega t - \pi/4 - x\sqrt{\frac{\omega}{2\alpha}}\right)}{2} \quad (4)$$

where A is the thermal oscillation magnitude calculated from Equation (1) and B can be extracted from a numerical analysis of the oscillation strength as a function of distance from the heater (Figure 2g). The magnitude of the third harmonic voltage oscillation can then be numerically approximated for different distances between the wires. Figure 3e,f shows the temperature oscillations calculated at 1 and 10 Hz for a distance D of 50, 42.5, and 57.5 μm , corresponding to 15% stretch and compression, respectively. The calculated signal at different distances is similar to the effect of applying strain to the heater, because the strain causes deformation in the serpentine shape, generally changing the spacing of repeated units. Due to the frequency dependence of the thermal penetration depth, the superimposed temperature oscillation at low frequency is expected to be higher than that at high frequency. The temperature oscillation that propagates from neighboring wires is, by calculation, roughly 31% at 1 Hz and 12% at 10 Hz, both of which overestimate the case of serpentine sensor, where the closest distance between repeated units is 50 μm . The changes in the temperature oscillations induced by 15% strain are roughly 3% at 1 Hz of the superimposed values. This explanation is consistent with the minor differences in temperature measured using serpentine heaters at 0% and 15% global applied strain (Figure 3g). In addition to effects of stretching, systematic measurements on silicone test samples reveal the effect of substrate curvature. Studies include measurements of temperature oscillations from a device laminated on PDMS cylinders with radii between 0.25 to 1.75 mm and on a flat PDMS substrate (Figure S5, Supporting Information). The effects of curvature throughout this range are less than 5.5% at 1 Hz, reducing further with increasing frequency (Figure S6, Supporting Information). The measurements at frequencies higher than 10 Hz have no effect on the extracted thermal properties. This relative insensitivity to curvature follows from the localized nature of the thermal actuation and the small sensing areas of the devices reported here (500 \times 250 μm). These results suggest robustness in operation on complex surfaces such as the skin, as described next.

The FEA method described previously can be used to evaluate thermal properties of various materials. For example, the thermal conductivity and diffusivity of water are fitted to be $0.63 \pm 0.04 \text{ W mK}^{-1}$ and $0.16 \pm 0.04 \text{ mm}^2 \text{ s}^{-1}$, consistent with reported literature values (Figure 3h,i).^[30,31] The FEA results presented as solid lines in Figure 3h match well with experimental results. The overall findings suggest a preference, in terms of simplicity in data interpretation, for 3ω sensors with serpentine geometries that have closest points of proximity that lie beyond the thermal propagation distance. Alternatively, arbitrary serpentine designs can be used with FEA to calculate thermal properties.

The soft, conformable 3ω sensors that follow from serpentine layouts can be broadly employed for measurement of thermal properties of various materials, ranging from rigid substances to soft biological tissues, such as skin. Here we utilize FEA models to extract thermal properties of skin at different body locations and physical conditions. The “epidermal” 3ω sensors can establish conformal contact with the epidermis in a manner that does not constrain or alter natural motions or behaviors of skin, without the need for separate bonding materials or externally applied pressures. Due to robust adhesion and conformality at the skin-device interface, the 3ω sensors can be laminated on various locations of the body to obtain thermal conductivity and diffusivity without causing irritation or discomfort. For example, in vivo measurements of the thermal conductivity and diffusivity of skin on the nose of a 22 year old female subject yield values of $0.42 \pm 0.02 \text{ W mK}^{-1}$ and $0.16 \pm 0.03 \text{ mm}^2 \text{ s}^{-1}$; the cheek has values of $0.42 \pm 0.02 \text{ W mK}^{-1}$ and $0.13 \pm 0.03 \text{ mm}^2 \text{ s}^{-1}$ (Figure 4a–c). Here, the skin is treated as an effective medium with a thickness of $\approx 60 \mu\text{m}$, including the epidermis and dermis of the skin. Additional demonstrations involve inducing dermatographic urticaria on the volar surface of forearm of a 22 year old female volunteer by a finger slap. The thermal properties change as a result of alterations in microvascular flow and local vasodilation. After urticaria, the thermal conductivity increases from 0.25 ± 0.02 to $0.33 \pm 0.02 \text{ W mK}^{-1}$ and the diffusivity increases from $0.15 \pm 0.03 \text{ mm}^2 \text{ s}^{-1}$ to $0.17 \pm 0.03 \text{ mm}^2 \text{ s}^{-1}$, consistent with previously reported trends.^[16] We also measured the thermal properties of skin at different hydrated states, and correlated the results to those determined with a moisture meter based on electrical impedance (Delfin MoistureMeterSC) (Figure 4g). Thermal conductivity increases in a linear fashion with an increase in hydration. The increase rate is around 0.03 W mK^{-1} per ten units of moisture level measured by the meter, which agrees with the literature (Figure 4h).^[15] By contrast, the change in the thermal diffusivity induced by hydration is within the standard deviation, much less compared to that in conductivity (Figure 4i). Therefore, the thermal conductivity or effusivity is the preferred thermal parameter to characterize the hydration state of the skin. The uncertainties in extracted values of the thermal conductivity and diffusivity can be defined by FEA results that yield $1.4\sigma_{\min}$, for an $\approx 95\%$ confidence interval.^[32] In general, the σ_{\min} is in the range of $(5\text{--}10}) \times 10^{-3}$. The results indicate significantly higher uncertainties in the thermal diffusivity than the conductivity. The overall uncertainties, including systematic uncertainty and fitting uncertainty, are less than 8% for thermal conductivity and 20% for thermal diffusivity.

3. Conclusion

The results presented here provide concepts and design principles for 3ω sensors that can be reversibly laminated onto a broad range of target materials, including biological tissues, for the purpose of accurate characterization of intrinsic thermal transport properties. While serpentine shaped sensors provide desired soft, stretchable mechanics, they also introduce a complication due to self-proximity effects of propagating thermal waves. Experimental results, FEA simulations and approximate numerical models support the theory that a superposition of thermal signals associated with the serpentine geometry alters the measured

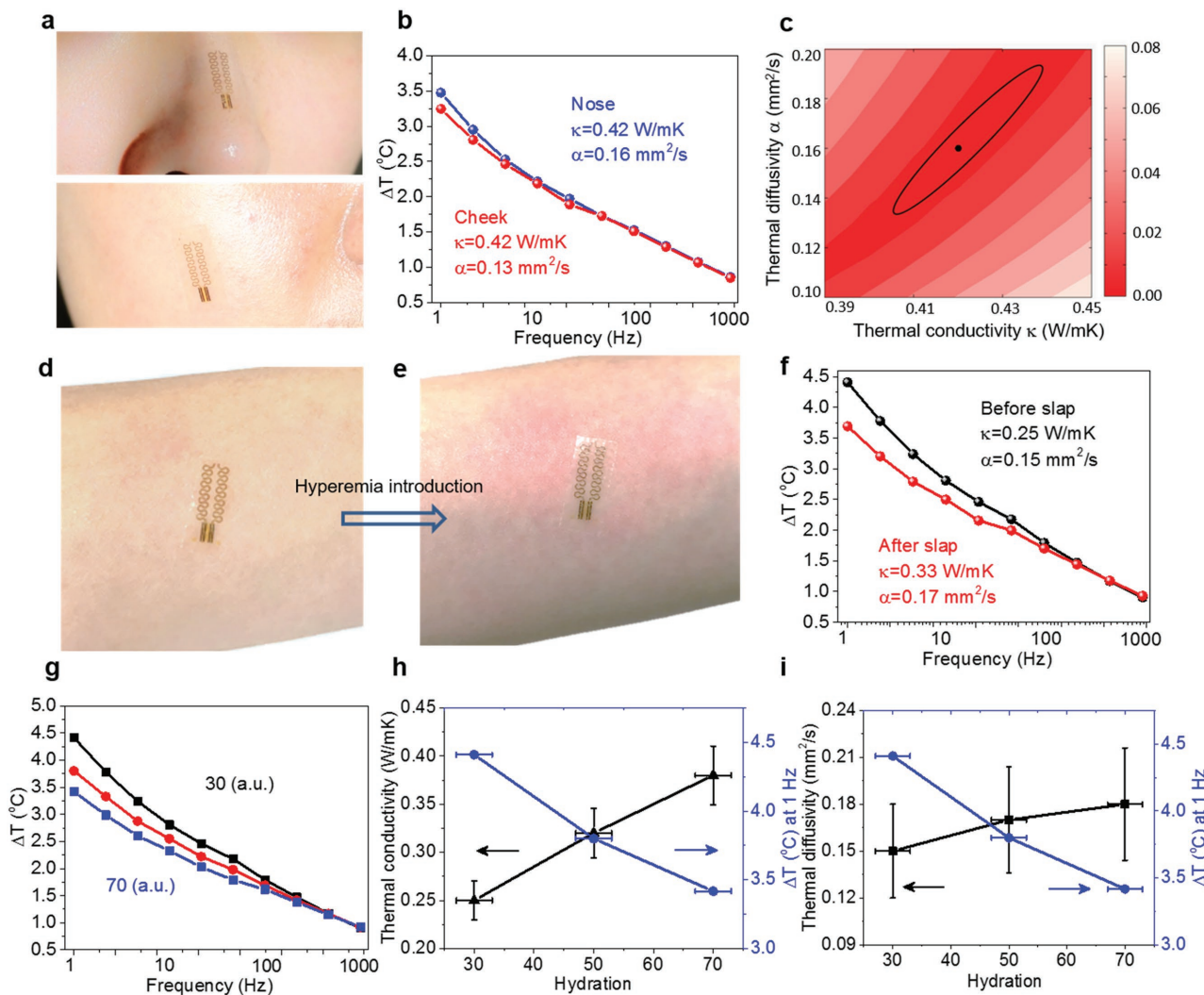


Figure 4. Thermal characterization of human skin. a) Photograph of a serpentine 3ω sensor laminated onto a human nose and cheek. b) Measured temperature oscillations from the serpentine wire in (a) as a function of frequency. c) The thermal conductivity and diffusivity of the skin of the nose, determined by extraction using FEA, are $0.42 \pm 0.02 \text{ W mK}^{-1}$ and $0.16 \pm 0.03 \text{ mm}^2 \text{ s}^{-1}$. Similarly, the thermal conductivity and diffusivity of the cheek are $0.42 \pm 0.02 \text{ W mK}^{-1}$ and $0.13 \pm 0.03 \text{ mm}^2 \text{ s}^{-1}$, respectively. d,e) Photographs of the forearm before and after slap-induced hyperemia and dermatographic urticaria. f) Measured temperature oscillations and calculated thermal properties of the skin before and after hyperemia. g) Measured temperature oscillations and calculated thermal properties of skin on the forearm at different hydrated states. h) Calculated thermal conductivity, i) thermal diffusivity, and temperature oscillation at 1 Hz as a function of skin hydration measured with a moisture meter.

third harmonic signals from that of a straight line-heater, but in a manner that can be accounted for in modeling. In particular, established finite element methods can accurately extract the thermal conductivity and diffusivity values of various materials from the measured data, including skin and other biological tissue under different conditions. These sensors can be envisioned in many contexts with relevance to human health, ranging from integration with surgical tools or implantable devices to use in noninvasive diagnostic and therapeutic applications.

4. Experimental Section

Fabrication of 3ω Sensors: A 450 nm layer of poly(methyl methacrylate) (PMMA 950 A7, Microchem, USA) spin cast on a 3 in. wafers served as

a sacrificial layer. Subsequently, a various spin casting yielded thin films of polyimide (PI-2545, HD Microsystems, USA; from 0.9 to 2 μm) on top of the PMMA, followed by soft baking and curing at 250 °C in an oven. Photolithographic patterning of bilayers of Cr (10 nm)/Au (100 nm) deposited by electron beam evaporation, defined the sensor and interconnects. A second layer of polyimide of the same thickness as the first layer placed the sensing/heating elements in the neutral mechanical plane and provided electrical insulation and mechanical strain isolation. Reactive ion etching of the polyimide defined the mesh layout of the array and exposed the bonding regions. A water-soluble cellulose tape enabled removal of the mesh from the Si wafer, to expose its back surface for deposition of Ti (5 nm)/ SiO_2 (50 nm) by electron beam evaporation. A silicone layer of 100 μm (Ecoflex, Smooth-On, USA) was spin cast onto a glass slide with its surface treated to reduce adhesion of the silicone. Subsequently, transfer of the device onto the silicone resulted in the formation of covalent bonds due to condensation reactions between SiO_2 and UVO treated silicone. After dissolving the cellulose tape with water,

a thin flexible conductive cable (HST-9805-210, Elform, USA) bonded to contacting pads of devices with desired heat and pressure as a connection to external electronics. The silicone sheet with the device removed from the glass slide produced a flexible and stretchable 3ω sensor.

Measurement Electronics for 3ω Sensing: The flexible cable from the thin film device connected to a custom printed circuit board that was wired to the measurement electronics. A precision AC current source (Keithley 6221, USA) supplied a sinusoidal current to the sensors and a digital lock-in amplifier (SR830, Stanford Research Systems, USA) recorded voltage signals of the third harmonic. The lock-in amplifier connected to the AC current source with phase locked via a 10 μ s TTL voltage pulse at each 0° phase passing of the current source. The lock-in amplifier was set with a 3 s settling time, high reserve, no line filters and a 24 dB roll-off filter. A custom computer program (LabVIEW, National Instruments, USA) controlled the lock-in amplifier and AC current source via a GPIB-USB interface.

FEA Modeling: For the straight Au wire, the FEA software ABAQUS established the heat transfer model for thermal analysis using DC2D4 element. The boundary condition was heat insulation on top of Ecoflex substrate and bottom of the sample. The temperature increase and heat flux were continuous across the interface between different layers. The input power corresponded to a surface heat flux introduced at the interface between two PI layers. The temperature increase in the Au wire was uniform because the thermal conductivity of Au (400 W mK $^{-1}$) is three orders of magnitude larger than that of the Ecoflex substrate (0.21 W mK $^{-1}$) and the PI layer (0.52 W mK $^{-1}$).^[27] For the serpentine Au wire, thermal analysis used 3D element DC3D8.

Experiments on Human Subjects: All experiments on humans were conducted under approval from Institutional Review Board at the University of Illinois at Urbana-Champaign (protocol number: 13920). There are two subjects (age: 20–22, female). Research was carried out with informed signed consent from the subjects.

Supporting Information

Supporting Information is available from the Wiley Online Library or from the author.

Acknowledgements

L.T., Y.L., and R.C.W. contributed equally to this work. Device fabrication and development were carried out in part in the Frederick Seitz Materials Research Laboratory Central Research Facilities, University of Illinois. L.T. acknowledges the support from Beckman Institute Postdoctoral Fellowship at UIUC. Y.L. acknowledges the support from the National Basic Research Program of China (Grant No. 2015CB351900). Y.H. acknowledges the support from NSF grant (Grant No. 1534120). Z.B. acknowledges the support from NSFC11572286.

Conflict of Interest

The authors declare no conflict of interest.

Keywords

3ω sensors, alternating current, epidermal electronics, thermal characterization

Received: March 9, 2017
Published online: May 15, 2017

- [1] D. G. Cahill, *Rev. Sci. Instrum.* **1990**, *61*, 802.
- [2] D. G. Cahill, H. E. Fischer, T. Klitsner, E. T. Swartz, R. O. Pohl, *J. Vac. Sci. Technol., A* **1989**, *7*, 1259.
- [3] C. Dames, G. Chen, *Rev. Sci. Instrum.* **2005**, *76*, 124902.
- [4] H. Natesan, W. Hodges, J. Choi, S. Lubner, C. Dames, J. Bischof, *Sci. Rep.* **2016**, *6*, 21395.
- [5] S. D. Lubner, J. Choi, G. Wehmeyer, B. Waag, V. Mishra, H. Natesan, J. C. Bischof, C. Dames, *Rev. Sci. Instrum.* **2015**, *86*, 014905.
- [6] N. O. Birge, *Phys. Rev. B* **1986**, *34*, 1631.
- [7] H. Ftouni, D. Tainoff, J. Richard, K. Lulla, J. Guidi, E. Collin, O. Bourgeois, *Rev. Sci. Instrum.* **2013**, *84*, 094902.
- [8] M. L. Bauer, P. M. Norris, *Rev. Sci. Instrum.* **2014**, *85*, 064903.
- [9] M. F. P. Bifano, J. Park, P. B. Kaul, A. K. Roy, V. Prakash, *J. Appl. Phys.* **2012**, *111*, 054321.
- [10] B. Feng, Z. X. Li, X. Zhang, G. P. Peterson, *J. Vac. Sci. Technol., B* **2009**, *27*, 2280.
- [11] S. M. Lee, *Rev. Sci. Instrum.* **2009**, *80*, 60.
- [12] C. Dames, G. Chen, *Rev. Sci. Instrum.* **2005**, *76*, 124902.
- [13] F. Chen, J. Shulman, Y. Xue, C. W. Chu, G. S. Nolas, *Rev. Sci. Instrum.* **2004**, *75*, 4578.
- [14] L. Qiu, D. W. Tang, X. H. Zheng, G. P. Su, *Rev. Sci. Instrum.* **2011**, *82*, 045106.
- [15] R. C. Webb, A. P. Bonifas, A. Behnaz, Y. Zhang, K. J. Yu, H. Cheng, M. Shi, Z. Bian, Z. Liu, Y.-S. Kim, W.-H. Yeo, J. S. Park, J. Song, Y. Li, Y. Huang, A. M. Gorbach, J. A. Rogers, *Nat. Mater.* **2013**, *12*, 938.
- [16] R. C. Webb, Y. Ma, S. Krishnan, Y. Li, S. Yoon, X. Guo, X. Feng, Y. Shi, M. Seidel, N. H. Cho, J. Kurniawan, J. Ahad, N. Sheth, J. Kim, J. G. Taylor VI, T. Darlington, K. Chang, W. Huang, J. Ayers, A. Gruebele, R. M. Pielak, M. J. Slepian, Y. Huang, A. M. Gorbach, J. A. Rogers, *Sci. Adv.* **2015**, *1*, 1500701.
- [17] R. C. Webb, R. M. Pielak, P. Bastien, J. Ayers, J. Niittynen, J. Kurniawan, M. Manco, A. Lin, N. H. Cho, V. Malyrchuk, G. Balooch, J. A. Rogers, *PLoS One* **2015**, *10*, e0118131.
- [18] C. Dames, *Annu. Rev. Heat Transfer* **2012**, *16*, 7.
- [19] B. W. Olson, S. Graham, K. Chen, *Rev. Sci. Instrum.* **2005**, *76*, 053901.
- [20] L. Gao, Y. Zhang, V. Malyarchuk, L. Jia, K.-I. Jang, R. Chad Webb, H. Fu, Y. Shi, G. Zhou, L. Shi, D. Shah, X. Huang, B. Xu, C. Yu, Y. Huang, J. A. Rogers, *Nat. Commun.* **2014**, *5*, 4938.
- [21] A. M. Stoll, *J. Invest. Dermatol.* **1977**, *69*, 328.
- [22] S. M. Brown, M. L. Baesso, J. Shen, R. D. Snook, *Anal. Chim. Acta* **1993**, *282*, 711.
- [23] J. A. Fan, W. H. Yeo, Y. W. Su, Y. Hattori, W. Lee, S. Y. Jung, Y. H. Zhang, Z. J. Liu, H. Y. Cheng, L. Falgout, M. Bajema, T. Coleman, D. Gregoire, R. J. Larsen, Y. G. Huang, J. A. Rogers, *Nat. Commun.* **2014**, *5*, 3266.
- [24] Y. W. Su, S. D. Wang, Y. A. Huang, H. W. Luan, W. T. Dong, J. A. Fan, Q. L. Yang, J. A. Rogers, Y. G. Huang, *Small* **2015**, *11*, 367.
- [25] L. Lu, W. Yi, D. L. Zhang, *Rev. Sci. Instrum.* **2001**, *72*, 2996.
- [26] N. Al-Khudary, P. Y. Cresson, Y. Orlic, P. Coquet, P. Pernod, T. Lasri, *Key Eng. Mater.* **2014**, *613*, 9.
- [27] Z. Hu, B. Carlberg, C. Yue, X. Guo, J. Liu, *presented at Int. Conf. on Electronic Packaging Technology & High Density Packaging (ICEPT-HDP '09)*, IEEE **2009**, pp. 10–13.
- [28] Y. Zhang, H. Fu, Y. Su, S. Xu, H. Cheng, J. A. Fan, K.-C. Hwang, J. A. Rogers, Y. Huang, *Acta Mater.* **2013**, *61*, 7816.
- [29] A. Ní Annaidh, K. Bruyère, M. Destrade, M. D. Gilchrist, M. Otténio, *J. Mech. Behav. Biomed. Mater.* **2012**, *5*, 139.
- [30] R. B. Montgomery, *J. Meteorol.* **1947**, *4*, 193.
- [31] J. V. Sengers, J. T. R. Watson, R. S. Basu, B. Kamgar-Parsi, R. C. Hendricks, *J. Phys. Chem. Ref. Data* **1984**, *13*, 893.
- [32] X. Wang, C. D. Liman, N. D. Treat, M. L. Chabinyc, D. G. Cahill, *Phys. Rev. B* **2013**, *88*, 075310.